

Hidden Latent State Inference in a Spatio-Temporal Generative Model

Matthias Karlbauer¹, Tobias Menge¹, Sebastian Otte¹,
 Hendrik P. A. Lensch², Thomas Scholten³, Volker Wulfmeyer⁴, Martin V. Butz¹

¹University of Tübingen – Neuro-Cognitive Modeling Group,
 Sand 14, 72076 Tübingen, Germany, martin.butz@uni-tuebingen.de

²University of Tübingen – Computer Graphics,
 Maria-von-Linden-Strae 6, 72076 Tübingen, Germany

³University of Tübingen – Soil Science and Geomorphology,
 Rümelinstrae 19-23, 72070 Tübingen, Germany

⁴University of Hohenheim – Institute for Physics and Meteorology,
 Garbenstrae 30, 70599 Stuttgart, Germany

Abstract

Knowledge of the hidden factors that determine particular system dynamics is crucial for both explaining them and pursuing goal-directed, interventional actions. The inference of these factors without supervision given time series data remains an open challenge. Here, we focus on spatio-temporal processes, including wave propagations and weather dynamics, and assume that universal causes (e.g. physics) apply throughout space and time. We apply a novel DIstributed, Spatio-Temporal graph Artificial Neural network Architecture, DISTANA, which learns a generative model in such domains. DISTANA requires fewer parameters, and yields more accurate predictions than temporal convolutional neural networks and other related approaches on a 2D circular wave prediction task. We show that DISTANA, when combined with a retrospective latent state inference principle called active tuning, can reliably derive hidden local causal factors. In a current weather prediction benchmark, DISTANA infers our planet’s land-sea mask solely by observing temperature dynamics and uses the self inferred information to improve its own prediction of temperature. We are convinced that the retrospective inference of latent states in generative RNN architectures will play an essential role in future research on causal inference and explainable systems.

Introduction

When considering our planet’s weather, centuries of past research have identified a large number of factors that affect its highly nonlinear and partially chaotic dynamics. Yet, can we ever be sure of having identified all hidden causal factors? Moreover, do we have (sufficient) data about them? These are fundamental questions in any prediction or forecasting task, including other spatio-temporal tasks such as soil property dynamics, traffic forecasting, energy-flow prediction (e.g. in brains or supply networks), or recommender systems. Here we investigate how unobservable hidden causes may be inferred from spatio-temporal data streams.

When regularities in hidden causes are detectable, they may be encoded in the latent activities of recurrent neural networks (Rodriguez, Alaniz, and Akata 2019; Rabinowitz et al. 2018), such as a long short-term memory (LSTM, Hochreiter and Schmidhuber 1997). The involved forward-directed inference, however, has two main disadvantages: First, the encodings of the hidden causes form while streaming data, meaning that they are not available from the beginning. Second, learning, detecting and shaping the encodings is relatively hard, because the error signal only decreases once the unfolding data stream is suitably compressed.

Here, we combine and extend the recently introduced DIstributed, Spatio-Temporal graph Artificial Neural network Architecture (DISTANA, Karlbauer et al. 2019) with active tuning (AT, Otte and Butz 2019; Butz et al. 2018, 2019), which enables the determination of hidden, latent, causal states via retrospective inference over both space and time. Projected onto stable hidden neural states, akin to parametric bias neurons (Tani, Ito, and Sugita 2004; Sugita, Tani, and Butz 2011), AT searches for constant input biases, assuming that the observed dynamics are influenced by particular, constant, unobservable factors.

Following the ideal of *relational inductive biases* (Battaglia et al. 2018), we work with DISTANA, which is designed to model the hidden causal processes that generate spatio-temporal dynamics. DISTANA assumes that the sensed dynamics are generated by general causal principles (e.g. physics). Moreover, we endow DISTANA with the expectation that constant, hidden latent factors modify the dynamic, spatio-temporal processes locally. For example, weather dynamics are locally dependent on the topology.

In the previous work of Karlbauer et al., it was shown that DISTANA can outperform two state-of-the-art models, ConvLSTM (Xingjian et al. 2015) and Temporal Convolution Network (TCN) (Bai, Kolter, and Koltun 2018), on a two-dimensional circular wave benchmark. Here, we apply DISTANA with AT to infer constant, hidden causal factors locally, even when these factors are never explicitly provided – neither as input nor as (target) output. As a result of both ar-

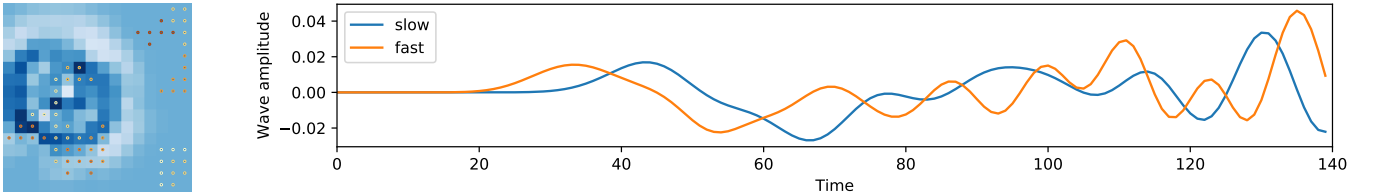


Figure 1: Left: two-dimensional wave propagating through a 16×16 grid with some obstacles. The darker the dot in a grid node, the larger its blocking effect on the wave. Right: the wave activity over time for two exemplary positions in the grid, with fast and slow propagation speeds.

chitectural and algorithmic improvements and optimizations, we show that latent static neural activities are inferred during training and testing exclusively via retrospective spatio-temporal analysis. Finally, to the best of our knowledge, we are the first to explore a graph neural network’s, that is DISTANA’s, ability to model global weather benchmark data (Rasp et al. 2020). After having learned a distributed, generative model of the globally unfolding dynamics, we demonstrate that our planet’s land-sea mask as well as other causal factors can be inferred via the retrospective analysis of unfolding weather dynamics – partially again even when the algorithm was never informed about these factors.

We conclude that the retrospective inference of latent states via AT offers a very powerful method to identify hidden causes in data streams and that graph neural networks bear great potential at modeling real-world spatio-temporal processes. In fact, we believe that the introduced principles are well-applicable to many other domains. While our inductive learning bias essentially assumes the presence of locally and temporally constant causal factors, modifications of these assumptions are possible and easy to implement.

Methods

We first introduce the considered benchmarks. Next, we detail the developed algorithms, focusing on DISTANA, its actual implementation in the light of the benchmarks, and the integration of AT.

Benchmarks and Datasets

The experiments are based on two spatio-temporal time series. Both are representatives of universal, but locally and temporally modifiable, spatio-temporal, causal processes that propagate dynamics over local topologies throughout a potentially heterogeneously connected graph.

2D Circular Wave Following Karlbauer et al., a spatio-temporal dataset was created to validate the correctness of our approach using a set of differential equations. More precisely, the two-dimensional wave equation was solved by means of the second order central differences method, resulting in an equation to calculate the elevation score for each position of the considered 16×16 -pixel field in the next time step (see Appendix for the equations used for data creation). This system of equations is used to initiate wave impulses (such as when dropping a stone into a lake) and then to simulate the wave expanding circularly outwards from this

point source, reflecting at borders, and interacting systematically with other crossing waves. In comparison to Karlbauer et al., the data generation was extended such that the wave propagation velocity could be contextually modified locally, which intuitively resembles obstacles in the water that affect the wave’s propagation behavior (see Figure 1). To train and evaluate the models, the classical mean squared error is used. This benchmark is used to (a) demonstrate and compare DISTANA’s principal capability of modeling locally parameterized spatio-temporal dynamics and (b) determine whether DISTANA can be used to infer an underlying and hidden static causal factor, which modifies the observed dynamics locally.

WeatherBench Recently, Rasp et al. introduced a benchmark for comparing mid-range (that is three to five days) weather forecast qualities of data driven and physics-based approaches. While the globally regularly aggregated data are provided in three spatial resolutions (5.625° , 2.8125° and 1.40525° resulting in 32×64 , 64×128 and 128×256 grid points, respectively), evaluated baselines are reported only for the coarsest resolution, which in consequence we chose too for elaborating and comparing DISTANA. Baselines are generated by means of persistence (tomorrow’s weather is today’s weather), climatology, linear regression and physics-based numerical weather prediction models. Moreover, convolutional neural networks (CNNs) are either applied iteratively or directly. Baselines are computed solely on the three or five day predictions of the geopotential at an atmospheric pressure level of 500 hPa (roughly at 5.5 km height, called Z500) and the temperature at 850 hPa (~ 1.5 km height, called T850). Beyond Z500 and T850, WeatherBench consists of numerous additional dynamic (humidity, ..., partially reported on multiple height levels and static (land-sea mask, topology, variables.

For training and testing, the following latitude weighted root mean squared error is applied, as proposed in Rasp et al.:

$$\text{RMSE} = \sqrt{\frac{1}{\#\text{lat}\#\text{lon}} \sum_i^{\#\text{lat}} \sum_j^{\#\text{lon}} L(i)(\hat{y}_{i,j} - y_{i,j})^2} \quad (1)$$

$$L(i) = \frac{\cos(\text{lat}(i))}{\frac{1}{\#\text{lat}} \sum_i^{\#\text{lat}} \cos(\text{lat}(i))}, \quad (2)$$

where $\#\text{lat}$ (latitude) and $\#\text{lon}$ (longitude) are the rows and columns of the two-dimensional lattice. In our case $\#\text{lat} = 32$

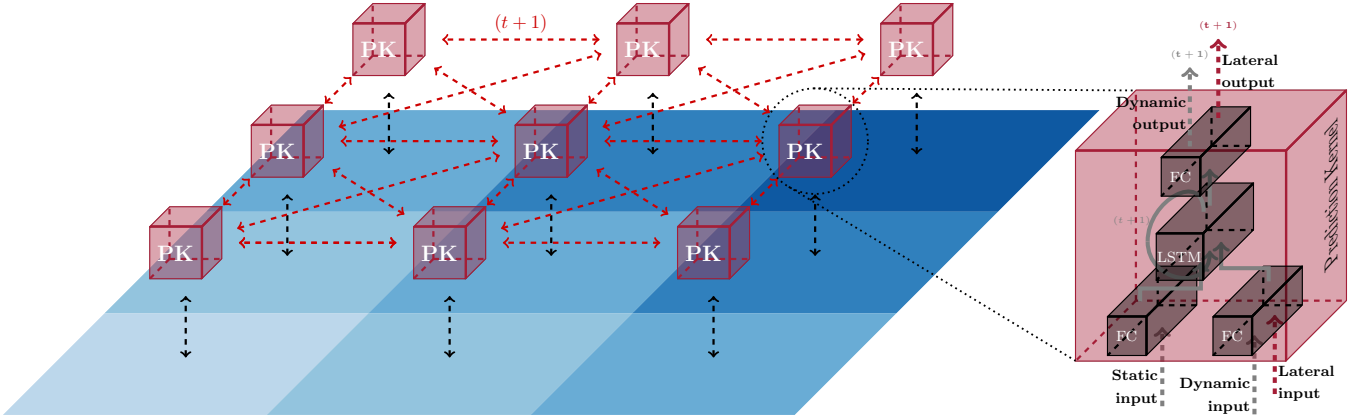


Figure 2: Left: 3×3 sensor mesh grid visualizing a 2D wave propagating from top right to bottom left and showing the connection scheme of Prediction Kernels (PKs) that model the local dynamical process while communicating laterally. Right: exemplary prediction kernel, receiving dynamic, static and lateral inputs, predicting dynamic output and producing lateral information flow.

and $\#lon = 64$, $y_{i,j}$ and $\hat{y}_{i,j}$ are the target and the model’s predicted value at the grid position (i, j) and $L(i)$ is the latitude weighting factor, which is largest at the equator (where $\text{lat}(i) = 0$) and decreases towards the poles (where $\text{lat}(i) \rightarrow \pm \frac{\pi}{2}$), such that errors in the equatorial regions – where the data distortions, coming from transforming the spherical data into a two-dimensional form, are minimal – contribute stronger to the overall error compared to errors at the poles.

We use weatherBench (a) to explore DISTANA’s capabilities at approximating real world phenomena by comparing it to Rasp et al.’s iterative CNN approach and (b) to investigate how to apply gradient-based inference techniques in order to infer local static context (such as e.g. the land-sea mask) that influences the Z500 and T850 dynamics.

State-of-the-Art

We compared DISTANA with two well-suited deep learning approaches. Firstly, we tested convolutional LSTMs (ConvLSTMs) (Xingjian et al. 2015) to predict the described circular wave dynamics. The network has 2 916 free parameters to project the $16 \times 16 \times 1$ input (ignoring batch and time dimensions) via the first layer on eight feature maps (resulting in dimensionality $16 \times 16 \times 8$) and subsequently via the second layer back to one output feature map. All kernels have a filter size of $k = 3$. They apply zero-padding and are implemented with a stride of one. Bias neurons were deactivated and code was taken and adapted from¹. Secondly, we tested Temporal Convolution Networks (TCN) (Bai, Kolter, and Koltun 2018; Dauphin et al. 2017; Kalchbrenner et al. 2016). The TCN used in this work is a three-layer network with 2 306 parameters, where the input layer projects to eight feature maps, which project their values back to one output value. A kernel filter size of $k = 3$ is used for the two spatial dimensions in combination with the standard dilation rate of $d = 1, 2, 4$ for the temporal dimension, resulting in a temporal horizon of 14 time steps, cf. (Bai, Kolter, and Koltun 2018). Various experiments with other sizes and deeper network structures have not yielded any better performance than the one reported here. Code was taken and adapted from Bai, Kolter, and Koltun.

iments with other sizes and deeper network structures have not yielded any better performance than the one reported here. Code was taken and adapted from Bai, Kolter, and Koltun.

DISTANA

As introduced in Karlbauer et al. and following the naming convention of Wu et al., DISTANA (the DIstributed Spatio-Temporal graph Artificial Neural network Architecture) can be described as a spatio-temporal graph neural network (GNN). While GNNs give the designer much freedom in controlling the information flow within the model (referred to as relational inductive biases) (Battaglia et al. 2018), they are reported to model physical systems with very high precision and accuracy for several hundreds of time steps even during closed loop prediction (Chang et al. 2016; Battaglia et al. 2016; Kipf et al. 2018; Sanchez-Gonzalez et al. 2018; Santoro et al. 2017; Van Steenkiste et al. 2018; Watters et al. 2017).

DISTANA consists of prediction kernels (PKs) that are arranged in a lattice structure. PKs model local dynamics concurrently. At each point in time t , they receive (i) local data and (ii) lateral output activities from the neighboring PKs from $t - 1$. The recurrent kernels then process this information, combine it with their previous latent state, and generate (i) predictions of the next data input at $t + 1$ as well as (ii) outputs to the laterally connected PKs (cf. Figure 2). PKs are akin to a spatio-temporal convolutional kernel: all PKs share the identical weights, that is, a single set of weights is applied and optimized over the entire grid. As a result, the likelihood of overfitting local data irregularities is tremendously reduced and a highly generalizing and universally applicable weight set develops. Moreover, less data is needed for training.

Modifying the LSTM Cell for Static Input In order to prevent the PKs from being excited by static input that does not change over time, DISTANA was modified such that, next to the regular dynamic input, static input can be provided,

¹https://github.com/nrplz/ConvLSTM_pytorch

which flows to the LSTM gates i^t, f^t, o^t only. Note, that the static input here corresponds to the previously mentioned context that locally modifies the observable process dynamics. The resulting forward pass of the adapted LSTM-based PKs – changes to the conventional LSTM are written in gray – is defined as:

$$i^t = \sigma(\mathbf{W}_X^i x^t + \mathbf{W}_S^i s^t + \mathbf{W}_H^i h^{t-1}) \quad (3)$$

$$f^t = \sigma(\mathbf{W}_X^f x^t + \mathbf{W}_S^f s^t + \mathbf{W}_H^f h^{t-1}) \quad (4)$$

$$o^t = \sigma(\mathbf{W}_X^o x^t + \mathbf{W}_S^o s^t + \mathbf{W}_H^o h^{t-1}) \quad (5)$$

$$u^t = \tanh(\mathbf{W}_X^u x^t + \mathbf{W}_H^u h^{t-1}) \quad (6)$$

$$c^t = i^t \odot u^t + f^t \odot c^{t-1} \quad (7)$$

$$h^t = o^t \odot \tanh(c^t), \quad (8)$$

where σ and \odot denote the sigmoid function and the pointwise (or Hadamard) product, respectively, \mathbf{W}_X^i connects the input x^t to the input gate i^t , \mathbf{W}_S^f the static input to the forget gate, \mathbf{W}_H^u encodes the recurrent weight matrix connecting the previous hidden state h^{t-1} to the LSTM input, and c^t is the LSTM cell's state in time step t . Note that no bias neurons are used, which additionally prevents spontaneous activities in spatial locations without actual wave signals.

Forward Pass of a PK Instance DISTANA, as proposed in this work, consists of a prediction kernel (PK) network, which is made up of the weight matrices $\mathbf{W}_{\text{pre}}^{DL}$, representing a dynamic- and lateral input preprocessing, $\mathbf{W}_{\text{pre}}^S$ as static input preprocessing, the weight matrices of our modified LSTM layer from above, and $\mathbf{W}_{\text{post}}^{DL}$, defining a dynamic- and lateral output postprocessing.

Given $k \in \mathbb{N}$ PK instances $\{p_1, p_2, \dots, p_k\}$, each of which having a list of eight neighbors $\mathbf{n}_i \in \mathbb{N}^8$, where each scalar $j \in \mathbf{n}_i, j \neq i$ refers to a neighboring PK instance p_j to p_i . Each PK instance p_i receives dynamic input $\mathbf{d}_i \in \mathbb{R}^d$, lateral input $\mathbf{l}_i \in \mathbb{R}^l$ from neighboring PK instances and optionally static input $\mathbf{s}_i \in \mathbb{R}^s$, with $d, l, s \in \mathbb{N}$ being the dimensionality of dynamic-, lateral- and static inputs, respectively. Since the PK contains an LSTM layer, it furthermore requires the hidden- and cell states $\mathbf{h}_i, \mathbf{c}_i \in \mathbb{R}^m$, where $m \in \mathbb{N}$ is the number of cells in the LSTM layer.

To perform the forward pass of PK instance p_i in time step t , the corresponding dynamic-, lateral- and static inputs $\mathbf{d}_i^{t-1}, \mathbf{l}_i^{t-1}, \mathbf{s}_i^{t-1}$, with $\mathbf{l}_i^{t-1} = \{\mathbf{l}_i | i \in \mathbf{n}_i\}$, along with the according LSTM hidden- and cell states $\mathbf{h}_i^{t-1}, \mathbf{c}_i^{t-1}$, are fed into the PK network to realize the following computations:

$$\mathbf{dl}_{\text{pre}} = \tanh(\mathbf{W}_{\text{pre}}^{DL}(\mathbf{d}_i^{t-1} \odot \mathbf{l}_i^t)) \quad (9)$$

$$\mathbf{s}_{\text{pre}} = \tanh(\mathbf{W}_{\text{pre}}^S \mathbf{s}_i^{t-1}) \quad (10)$$

$$\mathbf{c}^t, \mathbf{h}_i^t = LSTM(\mathbf{dl}_{\text{pre}}, \mathbf{s}_{\text{pre}}, \mathbf{c}_i^{t-1}, \mathbf{h}_i^{t-1}) \quad (11)$$

$$\mathbf{dl}_{\text{post}} = \tanh(\mathbf{W}_{\text{post}}^{DL} \mathbf{h}_i^t) \quad (12)$$

$$[\mathbf{d}_i^t | \mathbf{l}_i^t] = \mathbf{dl}_{\text{post}} \quad (13)$$

where vector concatenations are denoted by the \odot operator. As depicted in Equation 9 and Equation 12, the lateral input and output is processed by a fully connected nonlinear layer, leading to a potentially different treatment of the lateral information coming from any direction.

Gradient-based Inference Technique: Active Tuning

We modified active tuning (AT) (Otte and Butz 2019; Butz et al. 2018, 2019) to be applicable to two-dimensional data and used it to infer a local static context (potentially different at each grid position) in form of latent variables as model input that modify the observed dynamics. Essentially, AT can be seen as a different paradigm for handling RNNs: instead of the usual input \rightarrow compute \rightarrow output scheme, the RNN is decoupled from the direct input signal and instead is driven in closed-loop (it feeds itself with its own predictions). The RNN's dynamics are influenced by the input indirectly by means of temporal gradient information induced by the prediction error, that is, the discrepancy between the model output $\hat{\mathbf{y}}$ and a corresponding target signal \mathbf{y} .

The active tuning algorithm can be applied in combination with any desired gradient optimization strategy, e.g. Adam (Kingma and Ba 2014). Furthermore, the number of optimization cycles c and the history length H can be chosen, where the latter indicates up to what time in the past the latent context vector \mathbf{s} , which is assumed to be constant, is optimized.

Algorithm 1 Active Tuning

```

1: procedure ACTIVE TUNING( $H, c, \mathbf{x}, \mathbf{y}, \mathbf{s}$ )
2:   for  $c$  in range( $0, c$ ) do
3:     for  $t$  in range( $-H, 0$ ) do
4:        $\hat{\mathbf{y}}_t \leftarrow \text{model}(\mathbf{x}_t, \mathbf{s})$   $\triangleright$  Forward  $\mathbf{x}_t$  and  $\mathbf{s}$ 
      through the network to obtain  $\hat{\mathbf{y}}_t$ 
5:     end for
6:      $\mathbf{s} \leftarrow \mathbf{s} - \text{gradients}(\text{mse}(\mathbf{y}, \hat{\mathbf{y}}))$   $\triangleright$  Compute and
      apply gradients on  $\mathbf{s}$ 
7:   end for
8:   return  $\mathbf{s}$ 
9: end procedure

```

Experiments and Results

2D Circular Wave

If not specified elsewhere, Adam (Kingma and Ba 2014) is used for training with a learning rate of 10^{-3} . Network inputs \mathbf{x} and the according targets \mathbf{y} are exactly the same sequences shifted by one time step to train four different model types (ConvLSTM, TCN, DISTANA, DISTANA + AT) to iteratively predict the next two-dimensional dynamic wave field state.

Inferring Static Context DISTANA is augmented with a parametric bias neuron, whose activity is inferred during training and testing, aiming at the identification of an unknown location-specific wave velocity-influencing factor (static context). Results compare ConvLSTM, TCN, and DISTANA models. None of the models receive (the presumably unknown) information about the velocity-influencing factor values. Training was realized over 300 epochs consisting of 100 training sequences of length 70 each. For training, the static wave propagation speed vector \mathbf{s} of

MODEL	MSE
ConvLSTM	$(5.80 \pm 1.80) \times 10^{-2}$
TCN	$(4.02 \pm 4.01) \times 10^{-2}$
DISTANA	$(2.35 \pm 1.38) \times 10^{-3}$
DISTANA + AT	$(4.23 \pm 6.88) \times 10^{-4}$

Table 1: MSE results at test time confirm superior performance of DISTANA + AT when applied in the unknown static context scenario.

size 16×16 was generated by drawing values from $\{0.2, 0.3, 0.5, 0.6, 0.7, 0.9\}$; the smaller $s_{x,y}$, the slower the wave propagates at position x, y . The ground truth context map s_{GT} for training is visualized in Figure 1 (left, brownish dots). Note that, as stated above, s_{GT} was never provided to any model.

To smooth the context vector development during training, in each iteration t , a low pass filter was applied: $\hat{s}^t \leftarrow \alpha \cdot \hat{s}^t + (1 - \alpha) \cdot \hat{s}^{t-1}$ with $\alpha = 0.05$. Next, the static values were normalized (with respect to the mean and standard deviation over all spatial locations, that is, $\mu_{\hat{s}}$ and $\sigma_{\hat{s}}$): $\hat{s} = (\hat{s} - \mu_{\hat{s}}) / \sigma_{\hat{s}}$. Finally, values were clipped according to a 2.5σ -rule (with respect to moving average values of $\mu_{\hat{s}}$ and $\sigma_{\hat{s}}$) to suppress negative influences from outliers. These AT-modifications were crucial and enabled a reasonable inference of static inputs.

The preprocessing layer size of the DISTANA architectures was set to eight neurons, whereas the subsequent LSTM layer consisted of twelve cells, yielding 1 368 parameters. For the DISTANA + AT model, an additional static preprocessing layer with five neurons was used, which resulted in 1 394 weights overall, compared to 2 916 and 2 306 weights for ConvLSTM and TCN, respectively.

To test the models’ generalization capabilities, a new static context vector s' was generated, by drawing from all decimal values between 0.2 and 1.0, that is, $\{0.2, \dots, 1.0\}$ (see Figure 3, top right-most). All models were trained five times and evaluated on a test set consisting of 20 sequences made up of 140 time steps each. Reasonable activity was induced into the models by applying 50 steps of teacher forcing, followed by 90 steps of closed loop prediction for which an average MSE over all test examples and spatial locations was computed.

The prediction accuracy of ConvLSTM, TCN, DISTANA and DISTANA + AT differs considerably (see Table 1). While ConvLSTM and TCN tend to start oscillating increasingly after few steps of closed loop prediction, resulting in a mediocre MSE score, DISTANA, and DISTANA + AT in particular, preserve a stable activation pattern.

As shown in Figure 3 (bottom), DISTANA + AT preserves a linear ordering when indirectly inferring context values that were never encountered during training as can be seen at the ground truth static context values 0.4, 0.8 and 1.0, which are properly mapped to roughly 1.8, 0.2 and -0.5 , respectively, without violating the propagation speed order with other static context values. The static context map at test time, which is entirely different to the map on which the model was trained on, is inferred correctly without hardly any errors

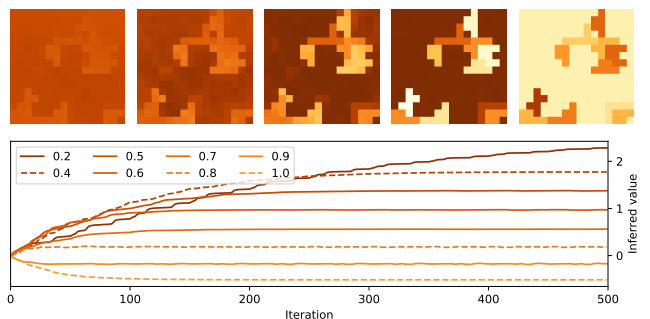


Figure 3: Top: inferred static context during testing after 5, 20, 80, 500 iterations and ground truth. Bottom: average inferred contexts over time during testing. While for the ground truth – values in the interval $[0, 1.0]$ – a darker color means a stronger blocking effect on the wave, the network inferred the context inversely in the interval of $[-0.5, 2.5]$, meaning that darker colors encode less blocking fields. Dashed lines show values that were not encountered during training.

(see image sequence of Figure 3, top). When comparing the prediction accuracy of DISTANA and DISTANA + AT, the self-inferred static context clearly helps DISTANA + AT to model the two-dimensional wave.

WeatherBench

Numerous experiments were conducted on weatherBench, focusing on the prediction of the previously mentioned Z500 (geopotential) and T850 (temperature) variables. All models (DISTANA and DISTANA + AT only) were trained for 2 000 epochs on weather data from 1979, using a learning rate of 10^{-4} , validated on 2016, and tested on 2017. Each year was partitioned into sequences of 96 hourly steps, yielding 91 sequences per year. Increasing the set sizes or changing the training, validation, or testing years did not seem to alter the results or model performances, which is in accordance with observations from other GNN research, where these models are observed to hardly ever overfit (Karl Bauer et al. 2019).

DISTANA’s preprocessing and LSTM layers were designed to have 50 neurons and cells, respectively. Furthermore, the implementation of DISTANA changed to support a varying lateral communication vector size, which then was increased from one to five neurons, to enable neighboring PKs to exchange information of higher complexity, yielding $\sim 25\,000$ parameters, slightly varying with the number of input variables.

Some static information provided by weatherBench was adapted and extended to facilitate the learning process. Changes were made to the latitude and longitude variables: latitude was transformed to being zero at the equator and non-linearly rising to one towards the poles, based on $\cos(\text{lat})$. The longitude variable was split into its sine and cosine component, generating a circular encoding. Additionally, one-dimensional north- and south-flags were provided to account for the missing neighbors in the north- and south-most rows in the grid. As has been done in Weyn, Durran, and Caruana, we also provide the top of atmosphere total incident solar

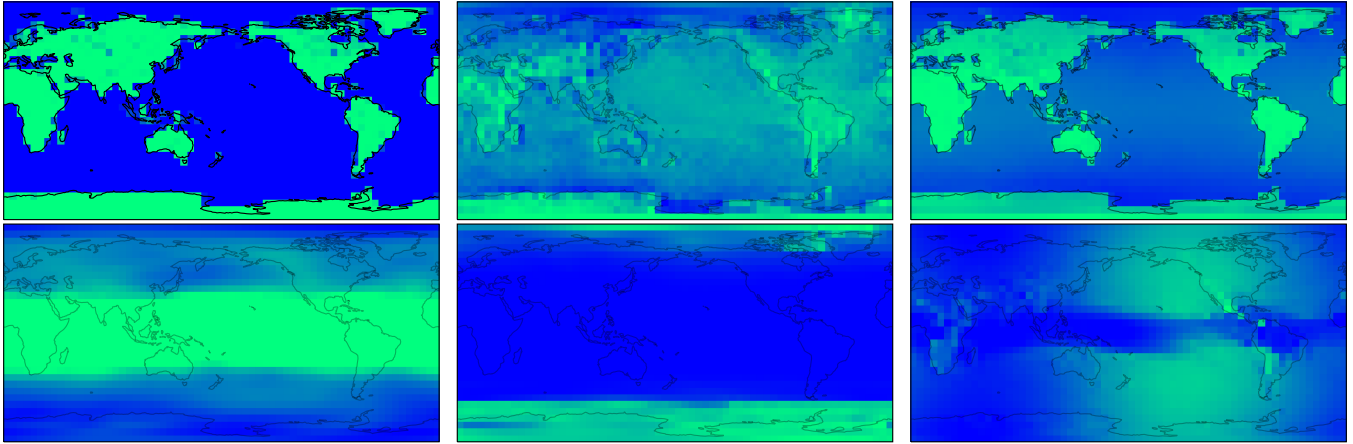


Figure 4: Top left: original land-sea mask (LSM). Top center: global LSM inferred during testing after being trained on two thirds of the globe (the model has never seen America’s LSM). Top right: latent vector which developed in training and clearly encodes LSM information as well as a decent latitude coding. Bottom: three latent variable codes that freely emerged during training of the Z500 (left, center) and T850 (right) variables.

radiation (t_{isr}). All variables were normalized to the range of $[-1.0, 1.0]$. When using AT to infer a latent static context \tilde{s} , the values were clipped to $[-1.0, 1.0]$ to prevent them from drifting or exploding.

If not specified differently, we provide the models with the dynamic variable Z500 or T850 (being subject for prediction), together with the following nine static inputs: orography, land-sea mask (LSM), soil type, longitude (two-dimensional), latitude, t_{isr} , and the north- and south-end flags.

Applying DISTANA to Real-World Data DISTANA was trained on real-world data for the first time, by providing the previously described nine-dimensional static input vector along with the Z500 variable for prediction.

The evaluation of DISTANA being trained to predict the Z500 variable after three days yielded an error of 816, which is clearly better than the current best comparable approach reported on the benchmark, which achieves an error of 1114. However, seeing that the best numerical weather prediction model produces an error of 154, we admit that there is room for improvement. Nonetheless, DISTANA offers the best learned generative, iterative processing model on the benchmark without applying techniques that reduce the distortion resulting from transforming the spherical Earth data to a regular two-dimensional grid.

Infering a Generalizable LSM Representation The second experiment was conducted to (a) investigate whether DISTANA + AT is capable of predicting the T850 variable and (b) simultaneously inferring missing LSM values just from the observed T850 dynamics during training. The model thus received the same static input as in the previous experiment along with the T850 variable during training. However, only two thirds of the LSM values were provided. The other third, considered missing values, which covered America and the Atlantic ocean, were to be inferred. After training, the

entire LSM vector \tilde{s} , initiated as zero vector, was retrospectively tuned via AT such that it best explains the observed dynamics.

As can be seen in Figure 4, top center, the LSM is inferred rather well, including America, which had to be inferred also during training, suggesting that the model learned a generalizable, globally applicable representation.

Infering Latent Variables In a third experiment, we used an additional latent neuron – a parametric bias neuron – that is locally tuned during training via AT. This latent neuron is supposed to be tuned freely by the model to develop any code that helps to predict the observed dynamics. Numerous conditions were evaluated, by either using the Z500 or the T850 variable for prediction and providing the network with or without land-coding variables (orography, LSM, soil type). We were particularly interested in evaluating whether DISTANA will develop latent states \tilde{s} that distinctively encode prediction-relevant, hidden causal factors. In this experiment, we try to answer the question what latent states are inferred depending on the predicted variable and how the presence of land-relevant input does affect the generation of this latent code.

Our results indicate that the nature of the developed latent states depends considerably on both the variable that is subject for prediction (Z500 or T850) and the additional static data provided. Figure 4 (top right) shows a tendency to encode land-sea information, augmenting it with a latitude code, when all previously mentioned static inputs (including LSM) were provided. In contrast, when training a model to predict Z500, the emerging latent variables rather seem to encode latitude, albedo, or humidity-distribution patterns (see Figure 4 bottom left and center). Excitingly, nuances of LSM and orography become visible when training to predict T850 without receiving any land-coding inputs (see Figure 4 bottom right). In other training runs, the inferred latent variable seemed to encode influences due to albedo, to monsoon, and

global humidity distribution patterns – but further studies are necessary to verify these observations in detail. It is also important to note that when local latent variables \tilde{s} are included to develop freely during training and testing, the prediction error of the network decreases slightly ($\approx 5 - 10\%$), but reliably.

Final Discussion

The presented results indicate that the combination of the Distributed, Spatio-Temporal graph Artificial Neural network Architecture, DISTANA, with retrospective inference mechanisms, which we call active tuning (AT), bears large potential at predicting spatio-temporal real-world phenomena (e.g. weather). It outperforms competing deep learning algorithms by generating more-accurate closed-loop predictions into the future. In addition, it can infer hidden causes by mere observation of a dynamic process. In particular AT in DISTANA is well-suited in inferring (i) contrastive hidden causes during learning and (ii) hidden static activities while minimizing loss online. AT optimizes neural activities by means of backpropagation through time, aiming at minimizing cumulative predictive loss in a faster manner than standard weight updates. As a result, network activities in form of latent codes get tuned in to the data stream and hidden, dynamics-influencing factors can be identified. While we believe that these hidden factors tend to encode causal influences – because they form for improving the accuracy of the predicted dynamics – future research will need to investigate the robustness of this tendency.

During learning, cumulative error signals in latent parametric bias neurons at the individual prediction kernels (PKs) tend to develop encodings of those factors. And to certain extend, the neuronal encodings resemble physical properties, such as albedo or the land-sea mask, depending on the type of dynamics that is to be predicted (e.g. temperature). During online prediction, when the network ideally is able to generate all possible dynamics in the analyzed data stream, the retrospective inference of recurrent, dynamic neural activities tunes the network dynamics in to the observed data streams. The projection of the gradient onto static neural activities identifies local parametric bias activities that best characterize the local, hidden causal factors. When projecting the gradient signal onto locally and temporally static neural activities, we essentially assume that hidden local factors exist that are constant and influence the unfolding spatio-temporal dynamics in a systematic manner. In the future, other assumptions about these hidden factors may be applied, such as a cyclic impulse, a basic wave pattern, or smoothly changing activities.

Overall, the results suggest that our approach of assuming and inferring hidden causes with constrained properties – such as being locally different, constant, but universally present – offers strong potential in fostering the development of process-explaining structures. Seeing that the introduced methods are generally complementary to standard training techniques and architectural network design, we are convinced that the application of suitable modifications of the introduced techniques to other domains still holds huge potential. Future research will show if this conjecture is correct.

Acknowledgments

This work received funding from the German Research Foundation (DFG) under Germany’s Excellence Strategy – EXC-Number 2064/1 – Project Number 390727645. Moreover, we thank the International Max Planck Research School for Intelligent Systems (IMPRS-IS) for supporting Matthias Karlbauer. Furthermore, we thank Georg Martius for valuable discussions and Maximus Mutschler for maintaining the GPU-cluster on which parts of this work’s experiments were conducted.

Appendix

2D Circular Wave Equations Similar to the work of Karlbauer et al., the 2D circular wave dataset was created by solving the two-dimensional wave equation

$$\frac{\partial^2 u}{\partial t^2} = c^2 \left(\frac{\partial^2 u}{\partial x^2} + \frac{\partial^2 u}{\partial y^2} \right) \quad (14)$$

by means of the second order central difference method

$$\frac{\partial^2 u}{\partial \beta^2} \approx \frac{u(\beta + h) - 2u(\beta) + u(\beta - h)}{h^2}. \quad (15)$$

Here, β is a placeholder for any variable of the wave function u – which in case of the wave equation is a function of space and time, that is $u(x, y, t)$ – and h is the step size of approximating the real function with the finite difference method. Note that we will abbreviate the second order derivative with $\partial^2 u / \partial v^2 := u_{vv}$ in the following. Applying Equation 15 to $u(x, y, t)$ and choosing Δ_t as approximation size for variable t results in

$$u_{tt}(x, y, t) \approx \frac{u(x, y, t + \Delta_t) - 2u(x, y, t) + u(x, y, t - \Delta_t)}{\Delta_t^2}. \quad (16)$$

Following Equation 14, we can write $c^2(u_{xx} + u_{yy})$ for $u_{tt}(x, y, t)$ in Equation 16 and solve for $u(x, y, t + \Delta_t)$ to obtain

$$u(x, y, t + \Delta_t) \approx c^2 \Delta_t^2 (u_{xx} + u_{yy}) + 2u(x, y, t) - u(x, y, t - \Delta_t), \quad (17)$$

with the velocity factor $c = 3.0$ and the temporal and spatial stepsizes $\Delta_t = 0.1$, $\Delta_x = \Delta_y = 1$, respectively.

The same finite difference method can be applied to u_{xx} and u_{yy} to come up with

$$u_{xx} \approx \frac{u(x + \Delta_x, y, t) - 2u(x, y, t) + u(x - \Delta_x, y, t)}{\Delta_x^2}, \quad (18)$$

analogously for u_{yy} . As in Karlbauer et al., the field is initialized with a 2D Gaussian around the origin of the wave, that is

$$u(x, y, 0) = a \exp \left(- \left(\frac{(x - s_x)^2}{2\sigma_x^2} + \frac{(y - s_y)^2}{2\sigma_y^2} \right) \right), \quad (19)$$

with s_x and s_y being the coordinates of the wave origin (where the stone drops into the water) and $\sigma_x^2 = \sigma_y^2 = 0.5$ determining the wave width in x - and y -direction. The boundary conditions are set to zero, that is

$$u(x, y, t) = \begin{cases} u(x, y, t) & \text{if } 0 \leq x \leq 15 \text{ and } 0 \leq y \leq 15 \\ 0 & \text{else} \end{cases}. \quad (20)$$

Ethics Policy

The overall goal of this work is to develop new methods for the prediction of complex dynamical systems, such as weather, in order to improve forecast qualities. While this would have a positive effect on numerous fields, such as e.g. agriculture or the economy, a critical aspect must be discussed: given the understanding of weather phenomena reaches a particular point from which on the dynamics of weather can be actively controlled, this ability gives rise to an enormous responsibility which must be taken seriously. This work, however, rather opens the field for a wide range of applications where unknown causes might be revealed and help to explain and develop more sophisticated models. Beyond the concrete applications reported in this paper, the presented techniques might help to determine unknown factors in any modeling problem and thus foster the explainability of certain processes and what they are composed of.

References

Bai, S.; Kolter, J. Z.; and Koltun, V. 2018. An empirical evaluation of generic convolutional and recurrent networks for sequence modeling. *arXiv preprint arXiv:1803.01271* .

Battaglia, P.; Pascanu, R.; Lai, M.; Rezende, D. J.; et al. 2016. Interaction networks for learning about objects, relations and physics. In *Advances in neural information processing systems*, 4502–4510.

Battaglia, P. W.; Hamrick, J. B.; Bapst, V.; Sanchez-Gonzalez, A.; Zambaldi, V.; Malinowski, M.; Tacchetti, A.; Raposo, D.; Santoro, A.; Faulkner, R.; et al. 2018. Relational inductive biases, deep learning, and graph networks. *arXiv preprint arXiv:1806.01261* .

Butz, M. V.; Bilkey, D.; Knott, A.; and Otte, S. 2018. REPRISE: A Retrospective and Prospective Inference Scheme. In *CogSci*.

Butz, M. V.; Menge, T.; Humaidan, D.; and Otte, S. 2019. Inferring Event-Predictive Goal-Directed Object Manipulations in REPRISE. *Artificial Neural Networks and Machine Learning – ICANN 2019* 11727: 639–653. doi:10.1007/978-3-030-30487-4_49.

Chang, M. B.; Ullman, T.; Torralba, A.; and Tenenbaum, J. B. 2016. A compositional object-based approach to learning physical dynamics. *arXiv preprint arXiv:1612.00341* .

Dauphin, Y. N.; Fan, A.; Auli, M.; and Grangier, D. 2017. Language modeling with gated convolutional networks. In *Proceedings of the 34th International Conference on Machine Learning – Volume 70*, 933–941. JMLR. org.

Hochreiter, S.; and Schmidhuber, J. 1997. Long short-term memory. *Neural computation* 9(8): 1735–1780.

Kalchbrenner, N.; Espeholt, L.; Simonyan, K.; Oord, A. v. d.; Graves, A.; and Kavukcuoglu, K. 2016. Neural machine translation in linear time. *arXiv preprint arXiv:1610.10099* .

Karlbauer, M.; Otte, S.; Lensch, H. P. A.; Scholten, T.; Wulfmeyer, V.; and Butz, M. V. 2019. A Distributed Neural Network Architecture for Robust Non-Linear Spatio-Temporal Prediction. *arXiv:1912.11141* .

Kingma, D.; and Ba, J. 2014. Adam: A Method for Stochastic Optimization. *International Conference on Learning Representations* .

Kipf, T.; Fetaya, E.; Wang, K.-C.; Welling, M.; and Zemel, R. 2018. Neural relational inference for interacting systems. *arXiv preprint arXiv:1802.04687* .

Otte, S.; and Butz, M. V. 2019. Active Tuning: Signal Denoising, Reconstruction, and Prediction with Temporal Forward Model Gradients. PCT/EP2019/069659, patent pending.

Rabinowitz, N.; Perbet, F.; Song, F.; Zhang, C.; Eslami, S. M. A.; and Botvinick, M. 2018. Machine Theory of Mind. In Dy, J.; and Krause, A., eds., *Proceedings of the 35th International Conference on Machine Learning*, volume 80 of *Proceedings of Machine Learning Research*, 4218–4227. Stockholm Sweden: PMLR. URL <http://proceedings.mlr.press/v80/rabinowitz18a.html>.

Rasp, S.; Dueben, P. D.; Scher, S.; Weyn, J. A.; Mouatadid, S.; and Thuerey, N. 2020. WeatherBench: A benchmark dataset for data-driven weather forecasting. *arXiv preprint arXiv:2002.00469* .

Rodriguez, R. C.; Alaniz, S.; and Akata, Z. 2019. Modeling Conceptual Understanding in Image Reference Games. In *Advances in Neural Information Processing Systems*, 13155–13165.

Sanchez-Gonzalez, A.; Heess, N.; Springenberg, J. T.; Merel, J.; Riedmiller, M.; Hadsell, R.; and Battaglia, P. 2018. Graph networks as learnable physics engines for inference and control. *arXiv preprint arXiv:1806.01242* .

Santoro, A.; Raposo, D.; Barrett, D. G.; Malinowski, M.; Pascanu, R.; Battaglia, P.; and Lillicrap, T. 2017. A simple neural network module for relational reasoning. In *Advances in neural information processing systems*, 4967–4976.

Sugita, Y.; Tani, J.; and Butz, M. V. 2011. Simultaneously emerging Brätenberg codes and compositionality. *Adaptive Behavior* 19: 295–316. doi:10.1177/1059712311416871.

Tani, J.; Ito, M.; and Sugita, Y. 2004. Self-organization of distributedly represented multiple behavior schemata in a mirror system: Reviews of robot experiments Using RNNPB. *Neural Networks* 17: 1273–1289.

Van Steenkiste, S.; Chang, M.; Greff, K.; and Schmidhuber, J. 2018. Relational neural expectation maximization: Unsupervised discovery of objects and their interactions. *arXiv preprint arXiv:1802.10353* .

Watters, N.; Zoran, D.; Weber, T.; Battaglia, P.; Pascanu, R.; and Tacchetti, A. 2017. Visual interaction networks: Learning a physics simulator from video. In *Advances in neural information processing systems*, 4539–4547.

Weyn, J. A.; Durran, D. R.; and Caruana, R. 2020. Improving data-driven global weather prediction using deep convolutional neural networks on a cubed sphere. *arXiv preprint arXiv:2003.11927* .

Wu, Z.; Pan, S.; Chen, F.; Long, G.; Zhang, C.; and Yu, P. S. 2019. A comprehensive survey on graph neural networks. *arXiv preprint arXiv:1901.00596* .

Xingjian, S.; Chen, Z.; Wang, H.; Yeung, D.-Y.; Wong, W.-K.; and Woo, W.-c. 2015. Convolutional LSTM network: A machine learning approach for precipitation nowcasting. In *Advances in neural information processing systems*, 802–810.